Transport in quantum spin Hall edges in contact to a quantum dot

Bruno Rizzo,[1] Alberto Camjayi,[1] and Liliana Arrachea[2]
[1]*Departamento de Física, Facultad de Ciencias Exactas y Naturales, Universidad de Buenos Aires, Pabellón I, Ciudad Universitaria, 1428 Buenos Aires, Argentina*
[2]*International Center for Advanced Studies, UNSAM, Campus Miguelete, 25 de Mayo y Francia, 1650 Buenos Aires, Argentina*
(Received 31 May 2016; revised manuscript received 25 August 2016; published 16 September 2016)

We study the transport mechanisms taking place in a quantum spin Hall bar with an embedded quantum dot, where electrons localize and experience Coulomb interaction U as well as spin-flip processes λ. We solve the problem with nonequilibrium Green functions. We focus on the linear-response regime and treat the many-body interactions with quantum Monte Carlo. The effects of U and λ are competitive and the induced transport takes place through different channels. The two mechanisms can be switched by changing the occupation of the dot with a gate voltage.

DOI: 10.1103/PhysRevB.94.125425

I. INTRODUCTION

The existence of metallic states at the boundaries of topological insulators (TIs) is one of the most appealing characteristics of these materials [1–3]. In the case of the two-dimensional (2D) systems, the edge states are helical (HESs) and exist in the form of Kramers' pairs of counterpropagating electron states with opposite spin [4–6]. These states are topologically protected [7] against disorder in the absence of time-reversal symmetry breaking factors such as a magnetic field [8] or magnetic impurities [9–11]. As a consequence, the transport is ideally ballistic and each pair of HESs supports a perfect conductance quantum $G_0 = e^2/h$. Recent experiments in HgTe quantum wells indeed provided evidence of the existence of 1D topological HESs [12–15].

The possibility of realizing electron interferometers in 2D TI bars, akin to those fabricated with quantum Hall edge states, captured significant attention [16–27]. Quantum interference is generated when tunneling processes between different Kramers pairs at opposite sides of the bar take place. The usual process is tunneling preserving spin, but the scenario is much richer when the tunneling with spin-flip also happens [16,20]. Such a scattering process does not break time-reversal symmetry and makes a helical interferometer different from two independent copies of a chiral electronic interferometer like those built in the quantum Hall regime.

Another relevant feature is the possibility of generating effective backscattering processes within the same Kramers' pair. This, in turn, generates effective resistive behavior with the concomitant departure of the conductance from the ideal quantum limit. A possible mechanism is the coupling of the HES to magnetic disordered impurities [28] or quantum dots representing puddles of the sample [29,30]. Indications of such resistive behavior has been actually experimentally observed, which adds motivation to a deeper understanding of this phenomenon. The coupling of helical edge states to quantum dots and magnetic impurities has been addressed in several works [28–42]. A crucial ingredient for a net resistive behavior to take place is an effective anisotropic coupling between the localized spins and the spins of the electrons in the HES.

In the present work we analyze the transport in helical edges of a 2D spin Hall bar with an embedded quantum dot. We focus on the combined effect of many-body interactions and local spin-flip processes taking place at the dot. The coupling between the edge states with such a quantum dot gives rise to backscattering and resistance within a Kramers' pair. It also generates effective tunneling processes between states at opposite edges of the bar preserving and flipping spin. We consider the setup sketched in Fig. 1, in which a quantum dot in the center of the bar is coupled to the HES. This may represent an antidot generated by a top gate as in quantum Hall systems [43] or a charge puddle of the sample. We analyze the impact of the different scattering mechanisms that may take place at the dot on the electron transport of this device. The work is organized as follows. In Sec. II we introduce the model and in Secs. III and IV the theoretical treatment. Section V is devoted to present results. Discussion and conclusions are presented in Sec. VI.

II. MODEL

The full setup of a spin Hall bar with four contacts is sketched in Fig. 1. This corresponds to a simplification of a six-terminal setup like the one studied in Ref. [14]. The latter setup contains left and right terminals, as well as two at the bottom and two at the top of the bar. Terminals (1) and (4) of the figure represent the two connected at the bottom, while (2) and (3) represent the two at the top of the bar in the six-terminal configuration. The bar also supports a quantum dot in the bulk, which can be generated by locally applying a gate voltage in a small region of the surface of the TI. As a consequence of the local voltage, Kramers pairs of edge states are originated enclosing the gate region. When the latter are close to the top and bottom edges of the bar, tunneling processes take place between the edge states of the dot and those of the bar. The corresponding Hamiltonian reads $H = H_0 + H_D + H_T$. The Hamiltonian for the electrons in the edge states is

$$H_0 = \sum_{\alpha=L,R} \sum_{\sigma=\uparrow,\downarrow} \int dx : \Psi^\dagger_{\alpha,\sigma}(x) \mathcal{D}_{\alpha,x} \Psi_{\alpha,\sigma}(x) : , \quad (1)$$

where x denotes a longitudinal coordinate and the integral is over the length of the edges. $\Psi_{\alpha,\sigma}(x)$ are fermionic fields describing electrons moving right and left along the edge ($\alpha = R, L$, respectively) with spin $\sigma = \uparrow, \downarrow$. Here $\mathcal{D}_{\alpha,x} = \mp i\hbar v_F \partial_x$

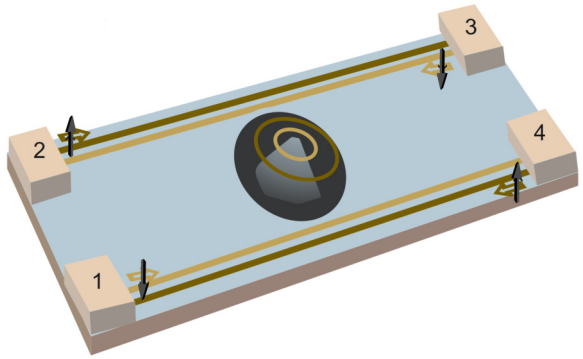

FIG. 1. Sketch for the setup of a quantum dot coupled to the edge channels of a topological insulator. The dot can be generated from the application of a negative gate voltage on the surface of TI. One direct consequence is the formation of localized states around the potential peak that mediates the different edge Kramers pairs. We assume that the coupling between the channels and the dot is punctual.

for $\alpha = L, R$ respectively while $:O:$ denotes normal ordering with respect to the state where all the states are filled up to the Fermi energy and v_F is the Fermi velocity. The quantum dot is modeled by an Anderson impurity model, where the helical edge states circulating around the local gate are represented by a localized electron level with the same energy ε_0 for electrons with up and down spin component,

$$H_D = \sum_{\sigma=\uparrow,\downarrow} \left[\varepsilon_0 d_\sigma^\dagger d_\sigma + \frac{U}{2} n_\sigma n_{\overline{\sigma}} + \lambda d_\sigma^\dagger d_{\overline{\sigma}} \right], \tag{2}$$

where U is the Coulomb repulsion for the electrons in the quantum dot and $\overline{\sigma}$ denotes the spin opposite to σ. The value of ε_0 is controlled by the local gate voltage. We also include a local spin-flip process in the dot by a phenomenological parameter λ [44–48]. Such a process may mimic the interaction of the localized spins at the dot with nuclear spins of the sample [35]. Another mechanism to realize such a term is by directly applying an external magnetic field transverse to the direction of the spin-orbit interaction of the 2D topological insulator. Finally, the term

$$H_T = \sum_{\alpha=R,L} \sum_{\sigma=\uparrow,\downarrow} \int dx \, [\Gamma(x) \Psi_{\alpha,\sigma}^\dagger(x) d_\sigma + \text{H.c.}], \tag{3}$$

with $\Gamma(x) = \frac{v_F \hbar}{\sqrt{d}} \gamma \delta(x - x_0)$, represents the spin-preserving tunneling between the dot and the edge states. Here d is a characteristic length of the contact.

III. TRANSPORT PROCESSES OF AN EDGE-STATE TERMINAL

We consider the configuration indicated in Fig. 1 where each of the four corners of the bar is contacted to independent reservoirs at which separate bias voltages can be applied. These four voltages enable an independent control on the injection of electrons into the four edge states. In what follows, we identify the terminal contacting the reservoir V_l with the label l. Each of these terminals hosts a Kramers pair of edge states containing a state incoming to the contact $(l+)$ and another one outgoing from it $(l-)$. Hence, the current flowing through a given terminal l is defined by the difference between the incoming and outgoing density of electrons [20],

$$I^l = -iev_F [G^<_{l+,l+}(x_l, x_l; t, t) - G^<_{l-,l-}(x_l, x_l; t, t)]. \tag{4}$$

There is a one to one identification between the labels $l+(-)$ and the labels of the helicity $(\alpha = R, L; \sigma = \uparrow, \downarrow)$. For instance, if we focus on the terminal 3, we see that $3+ \equiv R, \uparrow$ and $3- \equiv L, \downarrow$.

We define the Green function $G^<_{\alpha\sigma,\alpha'\sigma'}(x, x'; t, t') = i \langle \Psi^\dagger_{\alpha',\sigma'}(x', t') \Psi_{\alpha,\sigma}(x, t) \rangle$ and we present details on the calculation of this function in Appendix A. The resulting expression of the current can in general be decomposed as follows:

$$I^l = I^l_0 - I^l_{sp} - I^l_{sf} - I^l_b + I^l_{ne}. \tag{5}$$

The first term, $I^l_0 = \frac{e}{\hbar} \int_{-\infty}^{+\infty} \frac{d\omega}{2\pi} [f_{\alpha\sigma}(\omega) - f_{\overline{\alpha\sigma}}(\omega)]$, corresponds to purely ballistic transport through the terminal l in the absence of any coupling to the quantum dot. The associated conductance is $G_0 = e^2/h$. The other terms are due to the coupling to the quantum dot and tend to decrease the conductance with respect to the quantum limit G_0. The contributions I^l_{sp} and I^l_{sf} are due to the tunneling between different Kramers' pairs through the quantum dot preserving and flipping the spin respectively. The component I^l_b is an intrapair backscattering leading to an effective resistance in the terminal. The last term, I^l_{ne}, is a nonequilibrium contribution with components on the previous three channels. The explicit expressions for these different contributions are

$$\begin{aligned}
I^l_{sp} &= \frac{e}{h} \int_{-\infty}^{+\infty} d\omega \, \mathcal{T}^l_{\sigma,\sigma}(\omega) [f_{\alpha\sigma}(\omega) - f_{\overline{\alpha}\sigma}(\omega)], \\
I^l_{sf} &= \frac{e}{h} \int_{-\infty}^{+\infty} d\omega \, \mathcal{T}^l_{\sigma,\overline{\sigma}}(\omega) [f_{\alpha\sigma}(\omega) - f_{\alpha\overline{\sigma}}(\omega)], \\
I^l_b &= \frac{e}{h} \int_{-\infty}^{+\infty} d\omega \, \mathcal{T}^l_{\sigma,\overline{\sigma}}(\omega) [f_{\alpha\sigma}(\omega) - f_{\overline{\alpha\sigma}}(\omega)], \\
I^l_{ne} &= \frac{e}{h} \sum_{\sigma'=\sigma,\overline{\sigma}} \int_{-\infty}^{+\infty} d\omega \, \frac{d}{\gamma^2 v_F \hbar} \mathcal{T}^l_{\sigma,\sigma'}(\omega) \Lambda_{\sigma'}(\omega).
\end{aligned} \tag{6}$$

The functions

$$\mathcal{T}^l_{\sigma,\sigma'}(\omega) = \left(\frac{v_F \hbar}{\sqrt{d}} \gamma \right)^4 |g_{\alpha\sigma}(x_l, x_0; \omega)|^2 \left| G^R_{\sigma,\sigma'}(\omega) \right|^2 \tag{7}$$

characterize scattering processes where the electrons tunnel from the edge $\alpha\sigma$ to the quantum dot, eventually flip the spin (for $\sigma' = \overline{\sigma}$), and tunnel again to the edge $\alpha'\sigma'$. The Fermi function $f_{\alpha\sigma}(\omega)$ depends on the chemical potential and the temperature of the reservoir injecting the electrons into the edge $\alpha\sigma$. The function $g_{\alpha\sigma}(x_l, x_0; \omega)$ is the retarded Green function for the free edge state [see Eq. (B2)] while $G^R_{\sigma,\sigma'}(\omega)$ is the retarded Green function of the quantum dot coupled to the edge states. In the most general case, this function corresponds to the fully interacting quantum dot out of equilibrium. The function

$$\Lambda_\sigma(\omega) = 2 f_{\alpha\sigma}(\omega) \text{Im} \{ \Sigma^R_\sigma(\omega) \} + i \Sigma^<_\sigma(\omega) \tag{8}$$

is defined by the retarded and lesser components of the self-energy due to the Coulomb interaction at the dot, respectively, $\Sigma^R_\sigma(\omega)$ and $\Sigma^<_\sigma(\omega)$. This function vanishes close

to equilibrium, where all the chemical potentials and temperatures of the reservoirs are the same. In fact, the following fluctuation-dissipation relation holds: $2f(\omega)\mathrm{Im}\{\Sigma^R_\sigma(\omega)\} = -i\Sigma^<_\sigma(\omega)$. Hence, this process contributes to the current with a leading order $\propto V^2$, eV being the bias voltage applied at the terminals with respect to the reference chemical potential μ. Instead, the other three terms I^l_{sp}, I^l_{sf}, and I^l_b contribute at the linear order in the applied voltage V. In what follows, we will focus on small bias voltages where these contributions dominate. We will, thus, neglect the effect of I^l_{ne} and the Green function $G^R_{\sigma,\sigma'}(\omega)$ will be evaluated in the equilibrium system, as explained in Sec. IV.

For low temperatures and small bias voltages, the transport properties of the edge states in this setup are completed defined by the behavior of the function $\mathcal{T}^l_{\sigma,\sigma'}(\omega)$ close to the reference chemical potential μ. Because of the symmetry of this problem, the diagonal matrix elements of this matrix are identical, $\mathcal{T}_{\uparrow,\uparrow}(\omega) = \mathcal{T}_{\downarrow,\downarrow}(\omega)$ and also $\mathcal{T}_{\uparrow,\downarrow}(\omega) = \mathcal{T}_{\downarrow,\uparrow}(\omega)$. From Eq. (9) we directly see that the latter matrix elements vanish for $\lambda = 0$. Hence, if we focus on a particular terminal where the incoming edge is α,σ (for instance the terminal $l = 3$ at the upper right corner, which has $\alpha = R$ and $\sigma = \uparrow$), the effect of the spin-flip process will contribute to decrease the corresponding conductance due to backscattering processes when there is a bias applied from left to right ($\mu_1 = \mu_2 = eV + \mu$ and $\mu_3 = \mu_4 = \mu$). A similar behavior will be observed for the case of a bias applied from bottom to top ($\mu_1 = \mu_3 = \mu$ and $\mu_2 = \mu_4 = eV + \mu$) due to the interedge processes. On the other hand, in a configuration of voltages with $\mu_1 = \mu_2 = \mu_4 = \mu + eV$ and $\mu_3 = \mu$, we would get a current in the $l = 3$ terminal only due to the transmission without spin flip. In this way, a suitable selection of the voltages applied at the terminals will enable to gathering information of the different types of transport processes through the quantum dot. The transport behavior is fully described by the behavior of the two independent components of the transmission function $\mathcal{T}_{||} = \mathcal{T}_{\sigma,\sigma}(\mu)$ and $\mathcal{T}_\perp = \mathcal{T}_{\sigma,\bar{\sigma}}(\mu)$.

IV. GREEN FUNCTION OF THE QUANTUM DOT

In the previous section we have shown that the transport properties can be completely characterized within linear response in terms of two transmission functions, which depend on the retarded Green functions of the isolated edges and of the fully interacting quantum dot coupled to the edge states in equilibrium. The first ones can be analytically calculated and the explicit expressions are given in Appendix B. In this section we explain how to evaluate $G^R_{\sigma,\sigma'}(\omega)$. For the case of a noninteracting quantum dot, this function can be analytically evaluated while for the interacting case, we rely on numerical quantum Monte Carlo simulations. Below, we consider the two cases separately.

A. Quantum dot without Coulomb interaction

In the case where $U = 0$ it is possible to calculate the retarded Green function of the quantum dot coupled to the edge states analytically. In fact, we can readily solve the Dyson equation for the retarded Green function in this limit, by defining the matrix $\hat{G}^0(\omega)$ with matrix elements $G^0_{\sigma,\sigma'}(\omega) \equiv G^R_{\sigma,\sigma'}(\omega)$. The inverse of that matrix is

$$[\hat{G}^0(\omega)]^{-1} = [\omega - \varepsilon_0 - \Sigma_0(\omega)]\hat{\sigma}_0 - \lambda\hat{\sigma}_x, \tag{9}$$

where $\hat{\sigma}_0$ is the 2×2 unit matrix and $\hat{\sigma}_x$ is the x-Pauli matrix. We have also introduced the hybridization self-energy

$$\Sigma_0(\omega) = \left(\frac{\hbar v_F}{\sqrt{d}}\gamma\right)^2 \sum_{\alpha=L,R} g_\alpha(\omega) = -i\Gamma^0, \tag{10}$$

where $g_\alpha(\omega) \equiv g_{\alpha\sigma}(x_0,x_0;\omega)$ is the Green function of the free helical edge (the spin label was omitted since it is the same for both spin components) and $\Gamma^0 = \gamma^2\hbar v_F/d$.

B. Quantum dot with Coulomb interaction

For the fully interacting case, $U \neq 0$, we calculate the Green function in the Matsubara representation by recourse to quantum Monte Carlo. To this end we define the matrix $\hat{G}(i\omega_n)$ which is the inverse of

$$[\hat{G}(i\omega_n)]^{-1} = [\hat{G}^0(i\omega_n)]^{-1} - \hat{\Sigma}(i\omega_n), \tag{11}$$

where $\hat{G}^0(i\omega_n)$ is the Green function of the noninteracting quantum dot coupled to the leads (9) in the Matsubara axis while $\hat{\Sigma}(i\omega_n)$ is the self-energy matrix due to the Coulomb interaction U. These functions are calculated with quantum Monte Carlo by using the "continuous-time method" of Refs. [49–52]. In this method the Anderson impurity coupled to an arbitrary bath of free fermions can be computed in the Matsubara axis at finite temperature. The bath, which in our case is represented by the function (10), is an input of this algorithm. The retarded functions and the corresponding transport properties can be calculated by performing analytic continuation to the real frequency axis of Eq. (11) [53]. Here we focus on the features close to $\omega = \mu$, which are the relevant ones to evaluate the transmission functions $\mathcal{T}_{||}$ and $\mathcal{T}_\perp$ and we use the methodology of Refs. [54,55].

V. RESULTS

As discussed in Sec. III the transport properties of the setup are defined by the behavior of the components of the transmission function preserving and flipping spin, respectively, $\mathcal{T}_{||}$ and $\mathcal{T}_\perp$. In this section we analyze the effect of the different parameters of the model on the behavior of these functions. The relevant parameters are λ, U, and ε_0.

We fix the mean chemical potential of the reservoirs to $\mu = 0$ and start by fixing the local gate voltage of the dot to $\varepsilon_0 = -U/2$. In the noninteracting case ($U = 0$), this corresponds to the resonant level aligned with the Fermi energy of the edge states. In the interacting case, this corresponds to the dot occupied with a single electron, which is the typical scenario for the Kondo effect to take place. This effect is characterized by the coupling of the spin of the electron localized at the quantum dot with spins of the electrons of the edge states to form a singlet. This is accompanied by a fluctuation in the occupation, which effectively results in an electron resonance and a perfect transmission through the dot in the spin-preserving channel. This mechanism takes place only at low temperatures, below the so-called Kondo temperature [56,57]. In what follows, we fix the effective

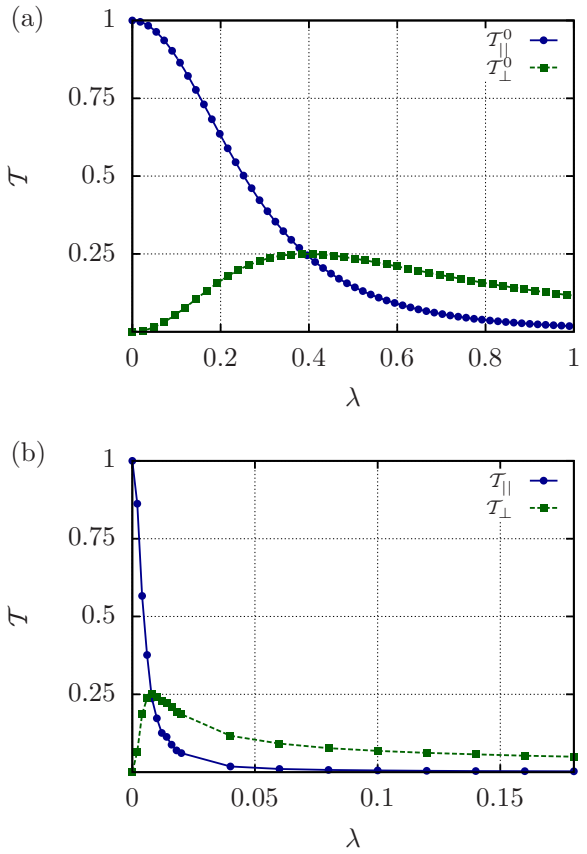

FIG. 2. Transmission functions at Fermi level vs the spin-flipping fluctuations λ for (a) noninteracting model ($U = 0$) with $\varepsilon_0 = 0$ and $\Gamma^0 = \pi/8$ and (b) interacting model with $U = 4$, $\varepsilon_0 = -U/2$, and $\Gamma^0 = \pi/8$. While (a) does not depend on temperature, the temperature in case (b) is $T = 0.0025$, being that the Kondo temperature is $T_K \simeq 0.013$ for these values of Γ^0 and U. All energies are expressed in units of $v_F\hbar/d$.

tunneling rate and focus on $U = 4$ and $\Gamma^0 = \pi/8$, which corresponds to a Kondo temperature $T_K \simeq 0.013$. The values of these quantities are expressed in units of $v_F\hbar/d$. In Fig. 2 we show the behavior of the transmissions as the spin-flip amplitude λ is varied. The top panel corresponds to the noninteracting quantum dot and the bottom panel to the quantum dot in the Kondo regime. The same global behavior is observed in both cases, namely, a decrease of the transmission preserving spin as the transmission with spin flip increases. In the noninteracting case, it is possible to write an analytical expression of the transmissions. In fact the different matrix elements of Eq. (9) read

$$G^0_{\sigma,\sigma}(\omega) = \frac{1}{g^{-1}(\omega) - \lambda^2 g(\omega)},$$
$$G^0_{\sigma,\bar{\sigma}}(\omega) = \frac{\lambda}{[g^{-1}(\omega)]^2 - \lambda^2}, \tag{12}$$

with $g^{-1}(\omega) = \omega - \varepsilon_0 + i\Gamma^0$. Substituting these expressions in (7) it is found that $\mathcal{T}_{||}$ is a decreasing function of λ with maximum $\mathcal{T}_{||} = 1$ for $\lambda = 0$ where $\mathcal{T}_{\perp} = 0$. Instead, $\mathcal{T}_{\perp}$ has a maximum at $\lambda = \Gamma^0$, where $\mathcal{T}_{\perp} = 1/4$. For the interacting case within the Kondo regime, it is natural to find a similar

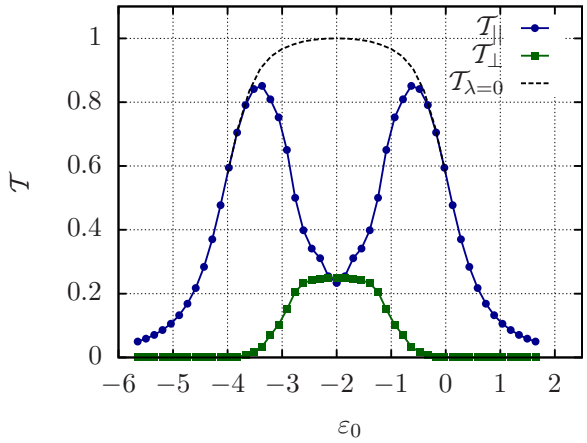

FIG. 3. Spin-preserving transmission $\mathcal{T}_{||}$ and spin-flipping transmission $\mathcal{T}_{\perp}$ at the Fermi energy vs the dot level ε_0. We fixed a low temperature $T = 0.0025$ to tune in the Kondo regime, setting $\lambda = 0.008$, $U = 4$, and $\Gamma^0 = \pi/8$.

behavior, since this is characterized by a resonance, as in the noninteracting case. This is indeed what we observe in Fig. 2(b). The results shown in this figure correspond to a temperature much lower than the Kondo temperature and basically correspond to the $T = 0$ limit. In fact, notice that for $\lambda = 0$ the function $\mathcal{T}_{||}$ achieves exactly the unitary limit. The scale at which the maximum of $\mathcal{T}_{\perp}$ and the strong decrease of $\mathcal{T}_{||}$ take place is, however, not set by the hybridization width Γ^0 as in the noninteracting case, but by the Kondo temperature T_K. This is because the width of the Kondo resonance is $\propto T_K$ and because the spin-flip processes and the formation of the Kondo singlet are competitive effects. Hence, for $\lambda \sim k_B T_K$ (k_B is the Boltzmann constant), the spin-flip process becomes dominant.

The effect of the gate voltage in the Kondo regime with spin-flip processes is analyzed in Fig. 3 for a particular value of λ close to the one for which $\mathcal{T}_{\perp}$ achieves the maximum for the symmetric configuration ($\varepsilon_0 \sim -U/2$) and a temperature much lower than the Kondo temperature. Interestingly, for values of $\varepsilon_0 \sim -U$ and 0, we observe a strong decrease of $\mathcal{T}_{\perp}$ while $\mathcal{T}_{||}$ displays two maxima approaching the unitary limit. The case without spin flip ($\lambda = 0$) is shown in dashed lines for comparison. It is characterized by the plateau with unitary transmission within the full interval $-U \leqslant \varepsilon_0 \leqslant 0$. These features can be understood by noticing that the gate voltage shifts the level of the quantum dot with respect to the Fermi energy of the edge states, leading to a change in its occupation. For $\varepsilon_0 = -U/2$ the dot is singly occupied, which is the optimal configuration for the Kondo effect to develop. As ε_0 departs from this value, the dot tends to be empty as $\varepsilon_0 \to 0$ or doubly occupied as $\varepsilon_0 \to -U$. On the other hand, the spin-flip term is effective only when the dot is singly occupied, in which case it competes with the Kondo effect. In this way, as the gate voltage approaches the limiting values $\varepsilon_0 = 0$ and $-U$, the spin-flip processes become ineffective and the transport takes place through the two levels separated by the energy U of the Coulomb-blockade regime. This is reflected in the behavior of the transmission functions, by the decreasing amplitude of

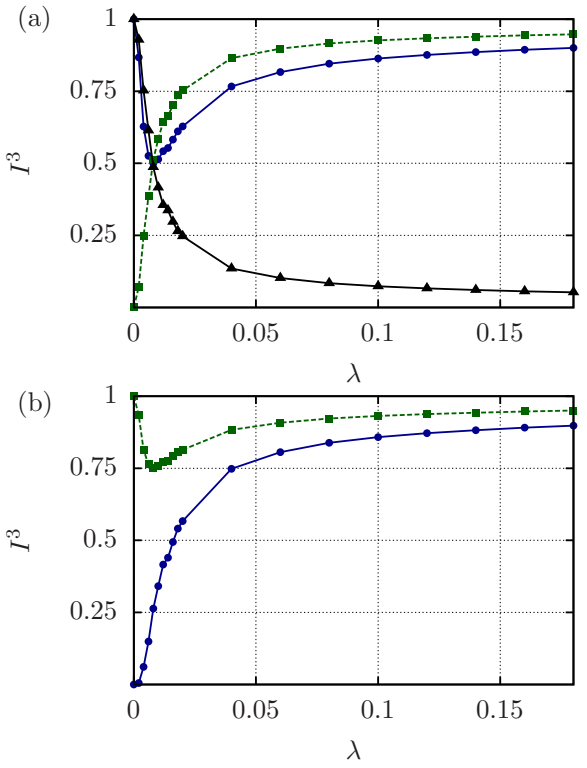

FIG. 4. Current in units of e^2V/h measured in terminal 3 vs the spin flipping parameter. (a) Bias voltage configuration: $\mu_2 = \mu_4 = eV$ and $\mu_1 = \mu_3 = 0$ (blue straight line with circles), $\mu_1 = \mu_2 = eV$ and $\mu_3 = \mu_4 = 0$ (green dashed line with squares), $\mu_1 = \mu_4 = eV$ and $\mu_2 = \mu_3 = 0$ (black solid line with triangles); (b) $\mu_2 = eV$ and $\mu_1 = \mu_3 = \mu_4 = 0$ (blue solid line with circles), $\mu_1 = \mu_2 = \mu_4 = eV$ and $\mu_3 = 0$ (green dashed line with squares). The rest of the parameters are the same as in Fig. 3

$\mathcal{T}_\perp$ as ε_0 departs from $-U/2$ and the increment of $\mathcal{T}_{||}$ to the limit of perfect transmission at $\varepsilon_0 = 0, -U$ observed in Fig. 3.

We analyze in Fig. 4 the behavior of the current measured at a given terminal as a function of the amplitude of the spin-flip processes. We consider the quantum dot in the half-filled configuration corresponding to $\varepsilon_0 = -U/2$ and we focus on the terminal at the top right corner of the 2D spin Hall bar, which is labeled with the index $l = 3$ (see Fig. 1). We consider different voltage configurations in order to separate and/or combine the different contributions of the transmission processes through the quantum dot. We begin by considering a bias configuration inducing colliding processes at the quantum dot. This corresponds to $\mu_2 = \mu_4 = eV$ and $\mu_1 = \mu_3 = 0$. The corresponding current is shown in the plot with blue circles of Fig. 4(a). For $\lambda = 0$ the current achieves its ballistic limit $I_0 = e^2V/h$. This is because, in the absence of spin-flip processes at the dot, the particle flow between HESs with same spin projection is forbidden due to the Pauli exclusion principle. In fact, as in this case $\mathcal{T}_\perp = 0$, the only component that could eventually contribute is the spin-preserving one I^l_{sp}, which depends on $\mathcal{T}_{||}$. However, we see from Eq. (6) that this component also depends on the difference of Fermi functions which vanishes for this voltage configuration. With increasing spin fluctuations at the quantum dot, the transmission with spin-flip $\mathcal{T}_\perp$ becomes active, opening the conducting channels I^l_b and I^l_{sf}. Hence, as λ increases, the net current decreases with respect to the ideal quantum limit I_0, achieving a minimum for the value of λ at which $\mathcal{T}_\perp$ has a maximum. As λ increases further, the spin fluctuations increase and deteriorate the low-energy resonance between the dot and HES. This is reflected in a smaller amplitude of $\mathcal{T}_\perp$, which leads to an increment of the current towards the quantum limit I_0. For $\mu_1 = \mu_2 = eV$ and $\mu_3 = \mu_4 = 0$ the bar is biased from the left to the right. The corresponding behavior of the current in the terminal $l = 3$ as a function of λ is shown in the green dashed plot with squares of Fig. 4(a). For $\lambda = 0$ the spin preserving current through the quantum dot is equal to the quantum limit $I^l_{sp} = I_0$ due to the perfect transmission $\mathcal{T}_{||} = 1$. This contribution exactly cancels the current injected by terminal 2 leading to a net vanishing current I^3. As λ increases, $\mathcal{T}_{||}$ decreases abruptly and new channels open with finite $\mathcal{T}_\perp$. The combination of the two contributions, however, is not enough to cancel the ballistic current and a finite net current flows through terminal 3, which increases in magnitude for increasing λ. Finally, the plot in black lines with triangles of Fig. 4(a) shows the behavior of the current I^3 for a bias applied from bottom to top, which corresponds to considering $\mu_1 = \mu_4 = eV$ and $\mu_2 = \mu_3 = 0$. In this case, the maximum current is found for $\lambda = 0$ due to perfect spin preserving transmission from the lower to upper channel. At finite values of λ, the contributions I^l_b and I^l_{sf} play a role, leading to a decreasing net current.

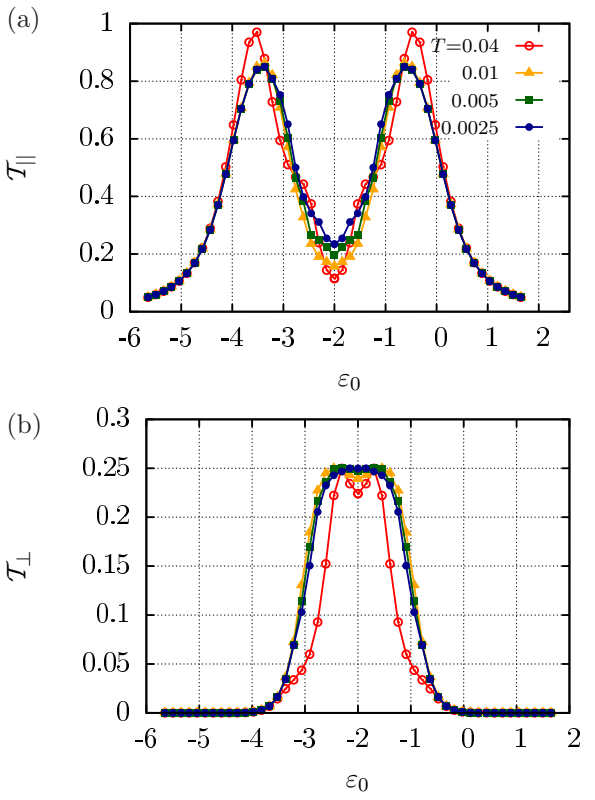

FIG. 5. Transmissions functions at the Fermi energy vs the dot level ε_0 for different temperature regimes. (a) Spin-preserving transmission $\mathcal{T}_{||}$. (b) Spin-flipping transmission $\mathcal{T}_\perp$ for the same parameters of Fig 3.

A similar analysis can be done for other voltage configurations corresponding to biasing one of the terminals against the other three. Examples are shown in Fig. 4(b). The case where $\mu_2 = eV$ and $\mu_1 = \mu_3 = \mu_4 = 0$ is shown in the blue-line plot with circles. For $\lambda = 0$ the perfect transmission $\mathcal{T}_{||}$ through the quantum dot causes a vanishing flow towards terminal 3. The effect of λ is to decrease $\mathcal{T}_{||}$, resulting in an increasing net current I^3. The other configuration shown in green lines with squares in Fig. 4(b) corresponds to $\mu_1 = \mu_2 = \mu_4 = eV$ and $\mu_3 = 0$. This voltage configuration is particularly interesting because it allows for measuring the effect of the backscattering component I_b independently from I_{sf}. In fact I_b vanishes for $\lambda = 0$ corresponding to the maximum $I^3 = I_0$, while the departure of I^3 from the perfect ballistic limit is precisely the backscattering component $I_b = I_0 - I^3$.

We close this section by analyzing the effect of the temperature in the features described in Fig. 3. This is shown in Fig. 5 within a range of temperatures below and above the Kondo temperature T_K. We see that the effect of the temperature is similar to the effect of the spin-flip processes regarding the behavior of the spin-preserving transmission $\mathcal{T}_{||}$, which tends to become smaller close $\varepsilon_0 = -U/2$ as T increases. Interestingly, the structure of $\mathcal{T}_{\perp}$ is more robust against changes in temperature. This indicates that the terms involving current transmission with spin inversion I_{sf} and the effective resistance I_b depends weakly on the temperature within the wide range of temperatures explored.

VI. CONCLUSIONS

We have analyzed the transport properties of the edge states of a 2D spin Hall bar in tunneling contact to a quantum dot where electrons are confined and experience Coulomb interaction U as well as local spin-flip processes λ. The occupation of the dot can be changed by means of a locally applied gate voltage ε_0. In the singly occupied quantum dot, under the Kondo temperature, the Kondo effect takes place along with the spin-flip processes. These two mechanisms are competitive and contribute to the transport along different channels.

The Kondo effect contributes to transport between two different Kramers pairs through the quantum dot without flipping the spin. The spin-flip term contributes to the effective tunneling with spin flip between the two Kramers pairs as well as within the same Kramers pair. The latter corresponds to an effective interpair backscattering and resistive behavior. By changing the gate voltage it is possible to change the occupation of the quantum dot. Away from single occupancy, the spin-flip term becomes ineffective and close to $\epsilon_0 = -U$ and 0, the transport takes place in the Coulomb blockade regime through the spin-preserving channel. The Kondo and the spin-flip processes are competitive, and the effect of one dominating over the other can be manipulated by the occupation. Hence, the gate voltage plays the role of a switch to select the spin-preserving or the spin-flip tunneling processes. Such a mechanism can be used to design helical interferometers like the ones discussed in Refs. [16–23]. In most of these references, the nontrivial effects on the conductance behavior were a consequence of tunneling with spin-flip between the HESs. In our case, we focused on local spin-flip processes at the quantum dot and concluded that this provides a channel for an effective tunneling process with spin flip between the HESs. In the case of coexisting both types of mechanisms, the combined effects with the Coulomb interaction as well as the consequences on the transport behavior would be qualitatively the same as the ones discussed in the previous section.

If we consider that typical realistic values for the Coulomb interaction and the hybridization function are similar to those in semiconductors [57], $U \sim$ 1–1.3 meV and $\Gamma \sim 0.1$ meV, then a very small value of the spin-flip parameter λ would lead to dramatic consequences in the transport properties below the Kondo temperature. For instance, notice that the plots of Fig. 3 correspond to $\lambda \sim 2 \times 10^{-3} U \sim 2\ \mu$eV. If, instead of an antidot as in the sketch of Fig. 1, the interacting region is a puddle as the one considered in Refs. [29,30,32], the effect of the flipping parameter would introduce a significant resistive behavior with the consequent reduction of the conductance in a six-terminal measurement like the one of Ref. [14]. This is an interesting outcome, since such a resistive behavior has been already experimentally observed.

ACKNOWLEDGMENTS

We acknowledge support by CONICET, MINCyT, and UBACyT from Argentina. L.A. acknowledges the hospitality of ICTP-Trieste and the support of a Simons associateship.

APPENDIX A: LESSER GREEN FUNCTION OF THE EDGE IN CONTACT TO THE QUANTUM DOT

We follow a similar approach to the one introduced in Ref. [20]. We summarize the main steps to derive the expression for the Green functions of the quantum dot. We start by defining the following Green functions in the Keldysh contour:

$$
\begin{aligned}
iG^{\mathcal{C}}_{\alpha\sigma,\alpha'\sigma'}(x,x';t,t') &= \langle T_{\mathcal{C}}[\Psi_{\alpha,\sigma}(x,t)\Psi^{\dagger}_{\alpha',\sigma'}(x',t')]\rangle,\\
iG^{\mathcal{C}}_{\alpha\sigma,\sigma'}(x;t,t') &= \langle T_{\mathcal{C}}[\Psi_{\alpha,\sigma}(x,t)d^{\dagger}_{\sigma'}(t')]\rangle,\\
iG^{\mathcal{C}}_{\sigma,\sigma'}(t,t') &= \langle T_{\mathcal{C}}[d_{\sigma}(t)d^{\dagger}_{\sigma'}(t')]\rangle,
\end{aligned}
\tag{A1}
$$

where $T_{\mathcal{C}}$ denotes temporal ordering along the Keldysh contour. These Green functions can be expressed in terms of retarded $G^R(t,t') = -i\theta(t-t')\langle[O(t),O^{\dagger}(t')]_+\rangle$ and lesser components $G^<(t,t') = i\langle O^{\dagger}(t')O(t)\rangle$ [58].

The contour-ordered functions obey the following Schwinger-Dyson equations, which when Fourier-transformed with respect to $t-t'$ lead to the following equations:

$$
\begin{aligned}
G^{\mathcal{C}}_{\alpha\sigma,\alpha'\sigma'}(x,x';\omega) &= \delta_{\sigma,\sigma'}g^{\mathcal{C}}_{\alpha\sigma}(x,x';\omega) + G^{\mathcal{C}}_{\alpha\sigma,\sigma'}(x;\omega)\\
&\quad\times\frac{v_F\hbar}{\sqrt{d}}\gamma g^{\mathcal{C}}_{\alpha'\sigma'}(x_0,x';\omega),\\
G^{\mathcal{C}}_{\alpha\sigma,\sigma'}(x;\omega) &= g^{\mathcal{C}}_{\alpha\sigma}(x,x_0;\omega)\frac{v_F\hbar}{\sqrt{d}}\gamma G^{\mathcal{C}}_{\sigma,\sigma'}(\omega).
\end{aligned}
\tag{A2}
$$

Substituting the second of these equations into the first one and evaluating the lesser component by applying the

Langreth rules for the complex contour [58], we find the expression for the lesser Green function for the edge channels:

$$G^{<}_{\alpha\sigma,\alpha\sigma}(x,x';\omega) = g^{<}_{\alpha\sigma}(x,x';\omega) + \frac{(\hbar v_F)^2}{d}\gamma^2\big[g_{\alpha\sigma}(x,x_0;\omega) \times G^{R}_{\sigma,\sigma}(\omega)g^{<}_{\alpha\sigma}(x_0,x';\omega) + g_{\alpha\sigma}(x,x_0;\omega)G^{<}_{\sigma,\sigma}(\omega)g^{*}_{\alpha\sigma}(x_0,x';\omega) + g^{<}_{\alpha\sigma}(x,x_0;\omega)G^{A}_{\sigma,\sigma}(\omega)g^{*}_{\alpha\sigma}(x_0,x';\omega)\big], \tag{A3}$$

where $G^{A}_{\sigma,\sigma}(\omega) = G^{R^*}_{\sigma,\sigma}(\omega)$ is the Fourier transform of the retarded Green function for the interacting dot coupled to the edge states and $g_{\alpha\sigma}(x,x';\omega)$ are the retarded Green functions of the free HESs. Explicit expressions for the latter are given in Appendix B. $g^{<}_{\alpha\sigma}(x_0,x_0;\omega) = -if_{\alpha\sigma}(\omega)\,2\,\mathrm{Im}\{g_{\alpha\sigma}(x_0,x_0;\omega)\}$ is the lesser Green function of the isolated HES and $f_{\alpha\sigma}(\omega)$ is the Fermi distribution that defines the filling of each edge channel α,σ.

In a similar, way, we can derive the following Green function for the dot in the Keldysh contour:

$$G^{\mathcal{C}}_{\sigma,\sigma'}(\omega) = g^{\mathcal{C}}_{\sigma,\sigma'}(\omega) + \sum_{\sigma''} G^{\mathcal{C}}_{\sigma,\sigma''}(\omega)\Sigma^{\mathcal{C}}_{\mathrm{tot},\sigma''}(\omega)g^{\mathcal{C}}_{\sigma'',\sigma'}(\omega),$$

where the total self-energy is $\Sigma^{\mathcal{C}}_{\mathrm{tot},\sigma}(\omega) = \Sigma^{\mathcal{C}}_{0,\sigma}(\omega) + \Sigma^{\mathcal{C}}_{\sigma}(\omega)$. The term

$$\Sigma^{\mathcal{C}}_{0,\sigma}(\omega) = \left(\frac{\hbar v_F}{\sqrt{d}}\gamma\right)^2 \sum_{\alpha=R,L} g^{\mathcal{C}}_{\alpha\sigma}(x_0,x_0;\omega) \tag{A4}$$

is due to the coupling to the edge states and the term $\Sigma^{\mathcal{C}}_{\sigma}(\omega)$ is due to the interaction U. By recourse to Langreth rules, we can calculate the lesser component of this function,

$$G^{<}_{\sigma,\sigma'}(\omega) = \sum_{\sigma''} G^{R}_{\sigma,\sigma''}(\omega)[\Sigma^{<}_{0,\sigma''}(\omega) + \Sigma^{<}_{\sigma''}(\omega)]G^{A}_{\sigma'',\sigma'}(\omega), \tag{A5}$$

with $G^{A}_{\sigma'',\sigma'}(\omega) = [G^{R}_{\sigma',\sigma''}(\omega)]^*$.

APPENDIX B: RETARDED GREEN FUNCTION OF THE ISOLATED HELICAL EDGE STATES

The Green functions of the free HESs are given by

$$g_{\alpha\sigma}(x,x';\omega) = \int_{-k_0}^{+k_0} dk\; g_{\alpha\sigma}(k;\omega)\,e^{ik(x-x')},$$
$$g_{\alpha\sigma}(k;\omega) = \frac{1}{\omega - v_\alpha\hbar k + i\eta}, \tag{B1}$$

where $v_\alpha \equiv s_\alpha v_F$ and $s_\alpha = 1\,(-1)$ for $\alpha = R\,(L)$. Taking the limit $k_0 \to \infty$, we obtain the following result:

$$g_{\alpha\sigma}(x,x';\omega) = \frac{-i}{v_F\hbar}\Theta[s_\alpha(x-x')]e^{i(s_\alpha/v_F\hbar)\omega(x-x')}. \tag{B2}$$

[1] S. Murakami, N. Nagaosa, and S.-C. Zhang, Phys. Rev. Lett. **93**, 156804 (2004).
[2] B. A. Bernevig, T. L. Hughes, and S.-C. Zhang, Science **314**, 1757 (2006).
[3] M. Z. Hasan and C. L. Kane, Rev. Mod. Phys. **82**, 3045 (2010).
[4] C. L. Kane and E. J. Mele, Phys. Rev. Lett. **95**, 226801 (2005).
[5] C. Wu, B. A. Bernevig, and S.-C. Zhang, Phys. Rev. Lett. **96**, 106401 (2006).
[6] C. Xu and J. E. Moore, Phys. Rev. B **73**, 045322 (2006).
[7] C. L. Kane and E. J. Mele, Phys. Rev. Lett. **95**, 146802 (2005).
[8] J. Maciejko, X.-L. Qi, and S.-C. Zhang, Phys. Rev. B **82**, 155310 (2010).
[9] J. Maciejko, C. Liu, Y. Oreg, X.-L. Qi, C. Wu, and S.-C. Zhang, Phys. Rev. Lett. **102**, 256803 (2009).
[10] Y. Tanaka, A. Furusaki, and K. A. Matveev, Phys. Rev. Lett. **106**, 236402 (2011).
[11] K. Hattori, J. Phys. Soc. Jpn. **80**, 124712 (2011).
[12] M. König, S. Wiedmann, C. Brüne, A. Roth, H. Buhmann, L. W. Molenkamp, X. L. Qi, and S.-C. Zhang, Science **318**, 766 (2007).
[13] M. König, H. Buhmann, L. W. Molenkamp, T. Hughes, C.-X. Liu, X.-L. Qi, and S.-C. Zhang, J. Phys. Soc. Jpn. **77**, 031007 (2008).
[14] A. Roth, C. Brüne, H. Buhmann, L. W. Molenkamp, J. Maciejko, X. L. Qi, and S.-C. Zhang, Science **325**, 294 (2009).
[15] T. Li, P. Wang, H. Fu, L. Du, K. A. Schreiber, X. Mu, X. Liu, G. Sullivan, G. A. Csáthy, X. Lin, and R.-R. Du, Phys. Rev. Lett. **115**, 136804 (2015).
[16] F. Dolcini, Phys. Rev. B **83**, 165304 (2011).
[17] R. Citro, F. Romeo, and N. Andrei, Phys. Rev. B **84**, 161301(R) (2011).
[18] F. Romeo, R. Citro, D. Ferraro, and M. Sassetti, Phys. Rev. B **86**, 165418 (2012).
[19] D. Ferraro, G. Dolcetto, R. Citro, F. Romeo, and M. Sassetti, Phys. Rev. B **87**, 245419 (2013).
[20] B. Rizzo, L. Arrachea, and M. Moskalets, Phys. Rev. B **88**, 155433 (2013).
[21] S.-P. Chao, T. L. Schmidt, and C.-H. Chung, Phys. Rev. B **91**, 235125 (2015).
[22] D. Ferraro, C. Wahl, J. Rech, T. Jonckheere, and T. Martin, Phys. Rev. B **89**, 075407 (2014).
[23] P. Sternativo and F. Dolcini, Phys. Rev. B **89**, 035415 (2014).
[24] C.-X. Liu, J. C. Budich, P. Recher, and B. Trauzettel, Phys. Rev. B **83**, 035407 (2011).
[25] F. Ronetti, L. Vannucci, G. Dolcetto, M. Carrega, and M. Sassetti, Phys. Rev. B **93**, 165414 (2016).
[26] P. Virtanen and P. Recher, Phys. Rev. B **83**, 115332 (2011).
[27] A. Mani and C. Benjamin, J. Phys.: Condens. Matter **28**, 145303 (2016).

[28] B. L. Altshuler, I. L. Aleiner, and V. I. Yudson, Phys. Rev. Lett. **111**, 086401 (2013).
[29] J. I. Väyrynen, M. Goldstein, and L. I. Glazman, Phys. Rev. Lett. **110**, 216402 (2013).
[30] J. I. Väyrynen, M. Goldstein, Y. Gefen, and L. I. Glazman, Phys. Rev. B **90**, 115309 (2014).
[31] G. Dolcetto, M. Sassetti, and T. L. Schmidt, Riv. Nuovo Cimento **39**, 113 (2016).
[32] F. Crépin, J. C. Budich, F. Dolcini, P. Recher, and B. Trauzettel, Phys. Rev. B **86**, 121106(R) (2012).
[33] G. Dolcetto, F. Cavaliere, D. Ferraro, and M. Sassetti, Phys. Rev. B **87**, 085425 (2013).
[34] S.-Y. Hwang, R. López, M. Lee, and D. Sánchez, Phys. Rev. B **90**, 115301 (2014).
[35] A. M. Lunde and G. Platero, Phys. Rev. B **86**, 035112 (2012).
[36] K. T. Law, C. Y. Seng, P. A. Lee, and T. K. Ng, Phys. Rev. B **81**, 041305 (2010).
[37] T. L. Schmidt, S. Rachel, F. von Oppen, and L. I. Glazman, Phys. Rev. Lett. **108**, 156402 (2012).
[38] V. Cheianov and L. I. Glazman, Phys. Rev. Lett. **110**, 206803 (2013).
[39] T. Posske, C.-X. Liu, J. C. Budich, and B. Trauzettel, Phys. Rev. Lett. **110**, 016602 (2013).
[40] T. Posske and B. Trauzettel, Phys. Rev. B **89**, 075108 (2014).
[41] B. Probst, P. Virtanen, and P. Recher, Phys. Rev. B **92**, 045430 (2015).
[42] A. Rod, G. Dolcetto, S. Rachel, and T. L. Schmidt, Phys. Rev. B **94**, 035428 (2016).
[43] M. Kataoka, C. J. B. Ford, M. Y. Simmons, and D. A. Ritchie, Phys. Rev. Lett. **89**, 226803 (2002).
[44] W. Rudzinski and J. Barnas, Phys. Rev. B **64**, 085318 (2001).
[45] R. López and D. Sánchez, Phys. Rev. Lett. **90**, 116602 (2003).
[46] M.-S. Choi, D. Sánchez, and R. López, Phys. Rev. Lett. **92**, 056601 (2004).
[47] B. Dong, G. H. Ding, H. L. Cui, and X. L. Lei, Europhys. Lett. **69**, 424 (2005).
[48] D. Sánchez, L. Serra, and M. S. Choi, Phys. Rev. B **77**, 035315 (2008).
[49] P. Werner, A. Comanac, L. de Medici, M. Troyer, and A. J. Millis, Phys. Rev. Lett. **97**, 076405 (2006).
[50] E. Gull, A. J. Millis, A. I. Lichtenstein, A. N. Rubtsov, M. Troyer, and P. Werner, Rev. Mod. Phys. **83**, 349 (2011).
[51] G. Kotliar, S. Y. Savrasov, K. Haule, V. S. Oudovenko, O. Parcollet, and C. A. Marianetti, Rev. Mod. Phys. **78**, 865 (2006).
[52] K. Haule, Phys. Rev. B **75**, 155113 (2007).
[53] L. Arrachea and M. J. Rozenberg, Phys. Rev. B **72**, 041301 (2005).
[54] A. Camjayi and L. Arrachea, Phys. Rev. B **86**, 235143 (2012).
[55] A. Camjayi and L. Arrachea, J. Phys.: Condens. Matter **26**, 35602 (2014).
[56] P. W. Anderson, Phys. Rev. **124**, 41 (1961).
[57] S. M. Cronenwett, T. H. Oosterkamp, and L. P. Kouwenhoven, Science **281**, 540 (1998).
[58] See H. Haug and A. P. Jauho, *Quantum Kinetics in Transport and Optics of Semiconductors*, Springer Series in Solid-State Sciences Vol. 123 (Springer-Verlag, Berlin, Heidelberg, 1996).